Applying virtual stent deployment to study flow-diversion treatment for intracranial aneurysms: the effect of stent compaction on post-treatment wire configuration

†*M. Zhang[1, 2], Y. Li[1, 2], D.I. Verrelli[1], W. Chong[3, 4], M. Ohta[5], and Y. Qian[1]

[1] Faculty of Medicine and Health Sciences, Macquarie University, Australia.
[2] Graduate School of Engineering, Tohoku University, Japan.
[3] Neuroradiology Department, Monash Medical Centre, Australia.
[4] Department of Surgery, Faculty of Medicine, Monash University, Australia
[5] Institute of Fluid Science, Tohoku University, Japan

[*] Presenting author: mingzi.zhang@biofluid.ifs.tohoku.ac.jp
[†] Corresponding author: mingzi.zhang@biofluid.ifs.tohoku.ac.jp

Abstract

Flow-diverting (FD) stent implantation has become a popular treatment mode for intracranial aneurysms (IAs). The stent wire configurations post-treatment can greatly affect the treatment outcomes. However, it remains a challenge to predict the stent wire configurations prior to a treatment. In this study, we propose to compare the FD stent structures and wire configurations between treatments with FD stents of different diameters being deployed at different compaction levels.

We adopted a recently reported spring–mass model to virtually implant FD stents of three diameters — 4.0, 4.5, and 5.0 mm, with each diameter modelled at three compaction levels (no compaction, a low compaction, and a high compaction) — into two clinically observed IAs: one successfully treated and the other unsuccessfully treated previously with a single FD stent. We then examined the morphological differences in stent wire configurations across different treatment scenarios, and quantified the porosity achieved in each such scenario.

This led us to two main findings. Firstly, at the same compaction level, the porosity differences attributable to device diameter were limited (SD < 2%). Secondly, stent deployment with some compaction could effectively reduce the FD wire porosity within the aneurysm ostium — a low compaction reduced the porosity by around 10%, and a high compaction reduced the porosity by around 30%.

The FD stent structures observed from virtual deployment can be used in the subsequent aneurysmal haemodynamic simulations. Thus, the virtual stent deployment strategy, together with the stent compaction measurement and simulation technique presented in this study, may contribute to research into flow-diversion treatment planning.

Keywords: Virtual stent deployment, Spring–mass model, Flow-diverting (FD) stents, Porosity, Treatment planning.

Introduction

Intracranial aneurysms (IAs) are common cerebrovascular disorders that can be identified as balloon-like dilations from a segment of brain artery [1, 2]. Untreated IAs can be dangerous, since subarachnoid haemorrhage could be induced due to aneurysm rupture. As an endovascular therapy, flow-diverting (FD) stent implantation is intended to reduce the blood velocity within the aneurysm sac, thereby promoting thrombotic occlusion of the aneurysm [2–4].

A favourable FD treatment outcome depends heavily upon sufficient flow diversion produced by the implanted device, whilst flow diversion is closely associated with the stent size and deployment procedure determined prior to a treatment [5]. Recently, stent deployment with a "push and pull" manoeuvre was introduced as an effective approach for a single stent to achieve lower porosity within the aneurysm ostium [6–8]. Along with other factors that may change the stent structure post-deployment (*e.g.* stent diameter), it remains a challenge to predict the stent wire configuration, so as to predict the treatment outcomes.

In this study, we propose to investigate the procedure of stent deployment when a compaction technique is applied, and to quantify the stent wire porosity post-deployment across various treatment scenarios. To realise this objective, we employed a numerical method for virtual stent deployment simulation. Furthermore, we defined a variable to characterise the level of stent compaction, to enable quantitative assessments to be made. Adopting these approaches, we examined a total of 18 deployment procedures for two patient-specific aneurysms, considering different combinations of stent diameter and compaction ratio.

Methods

Patient Aneurysm Geometries and Model FD Stent

We accessed the patient aneurysm geometries after institutional ethics approval was granted. Two patient aneurysms were studied — one successfully treated case in which complete aneurysm occlusion was confirmed 6 months after treatment, and the other an unsuccessfully treated case in which an aneurysm lobule was identified by digital subtraction angiography (DSA) scans. Both patients were treated with the commercially available *Silk+* stent (Balt Extrusion, Montmorency, France).

The *Silk+* stents comprise a total of 48 braided Nitinol-alloy filaments, with each filament having an average diameter of 35 μm [9]. We employed a fast geometric deployment approach — the spring–mass analogue [10–13] — in the simulation of FD stent deployment. In this spring–mass analogue, a series of assumptions were adopted:

1) the FD wire filaments were represented by a group of centreline trajectories without an explicit thickness;
2) the intersections of FD wire filaments were assumed to be mass points (nodes), which were connected with each other by fictitious springs based upon the topology of the FD stent being modelled;
3) the stiffness of each spring was related to the length and thickness of the FD wire filament being represented.

With these simplifications applied, the internal force of a *Silk+* stent could be calculated following the 3D Hooke's law:

$$F_i = \sum_{j=1}^{n_i} k_{ij}\left(\delta_j - \delta_i\right), \tag{1}$$

in which δ_i and δ_j refer to the displacements of nodes i and j; k_{ij} denotes the stiffness of the fictitious spring connecting node i and its neighbour j; and n_i is the number of nodes directly connected to node i.

Virtual Stent Deployment

The *Silk+* stent was assumed to be initially crimped in alignment with the centreline of the parent artery, and then expanded to its unloaded condition. The expansion process was driven by the internal restoring forces from the mass points, and was constrained by vascular geometries — the arterial wall, *etc*. To constrain the nodal movements within the boundaries of the parent artery, a wall-touch detection algorithm was invoked after each step of nodal movement. The benchmark of simulation convergence was set as the displacement of each mass point being less than 1 μm after a step of nodal movement.

Measurement of the Compaction Ratio

The stent compaction ratio was measured in accordance with the maximum compaction length ΔL_{max} of a FD stent, a parameter defined as the maximum longitudinal distance that an additional length of FD stent could possibly be compacted into the aneurysm neck segment. The parameter ΔL_{max} was calculated as

$$\Delta L_{\text{max}} = \left(\frac{p_1}{p_{\text{min}}} - 1 \right) \cdot L_{\text{neck}}, \tag{2}$$

where L_{neck} denotes the longitudinal length of the aneurysm neck segment, p_1 is the helical filament pitch of a FD stent in the neutrally expanded condition, prior to compaction, and p_{min} is the filament pitch in the fully compacted condition, *i.e.* in a condition where no space exists between any two neighbouring wires and the metal coverage ratio (MCR) therefore equals 100%. By letting MCR = 100%, p_{min} could be calculated from

$$\text{MCR (\%)} = \frac{nd\sqrt{p^2 + \pi^2 D^2}}{\pi p D} \times 100, \tag{3}$$

where n is the number of FD wire filaments; d is wire thickness; and D denotes the nominal diameter of a FD stent. The stent compaction ratio could therefore be computed as

$$\text{CPT} = \frac{\Delta L}{\Delta L_{\text{max}}} \tag{4}$$

We investigated FD stent deployment under three conditions: non-compacted (CPT = 0%), low-compacted (CPT = 20%), and high-compacted (CPT = 70%) conditions.

Results

Virtual Stent Deployment Procedures

Figures 1 and 2 demonstrate the representative deployment procedures for the successful and the unsuccessful case. As can be observed from the stent deployment procedures, FD stents expand progressively from the initial fully crimped condition to the final fully expanded condition, controlled by the boundaries of the aneurysm's parent artery.

FD Stent Structures and Wire Configurations

Figures 3 and 4 depict the FD stent structures and wire configurations after treatments with FD stents of three diameters deployed at three compaction ratios. Both figures show that: (i) the length of a FD stent becomes shorter when the stent is subjected to compaction during deployment; and (ii) the mesh density within the aneurysm ostium becomes higher when a higher compaction is applied during FD stent deployment.

Figure 5 presents the values of stent porosity within the aneurysm ostium measured from treatments using the default deployment technique (CPT = 0%), and following the deployments with a low compaction (CPT = 20%) and a high compaction (CPT = 70%). Regardless of compaction levels, the porosities obtained in the unsuccessfully treated case were higher than those obtained in the successful one. However the differences attributable to the device's diameter were modest, with a standard deviation (SD) less than 2%. Compared to the default stent deployment, deployment with a low compaction reduced the average porosity from 72.5% to 64.2 % for the successful case, and from 76.3% to 69.3% for the unsuccessful case. In addition, stent deployment with a high compaction further reduced the porosities by 20% (on average), compared to the low compaction conditions in both cases.

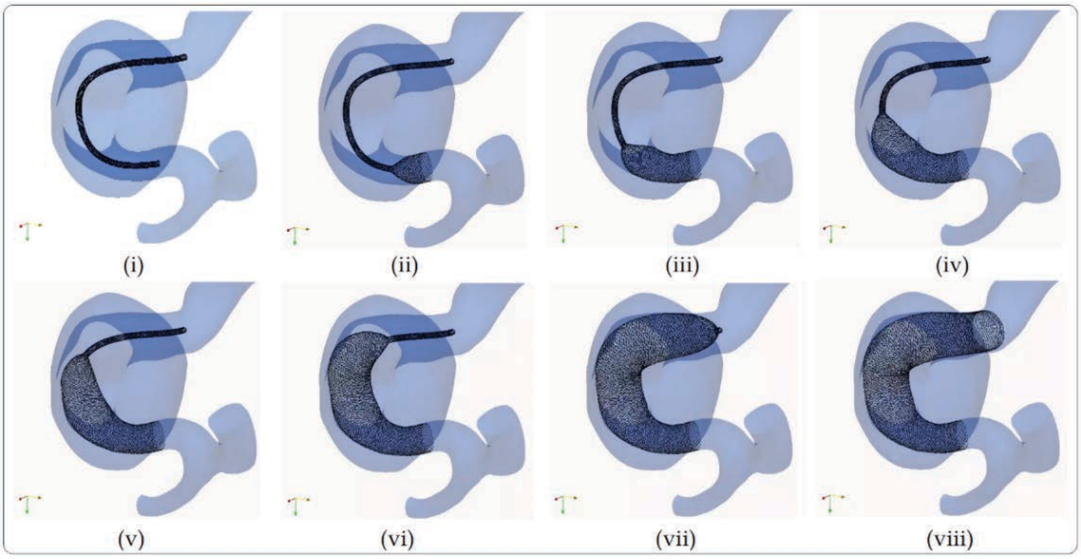

Figure 1. A representative virtual stent deployment procedure for the successfully treated aneurysm. (FD stent size: 4.5 mm, under non-compacted condition; subfigures i to viii: the deployment procedure from stent fully crimped to stent fully expanded.)

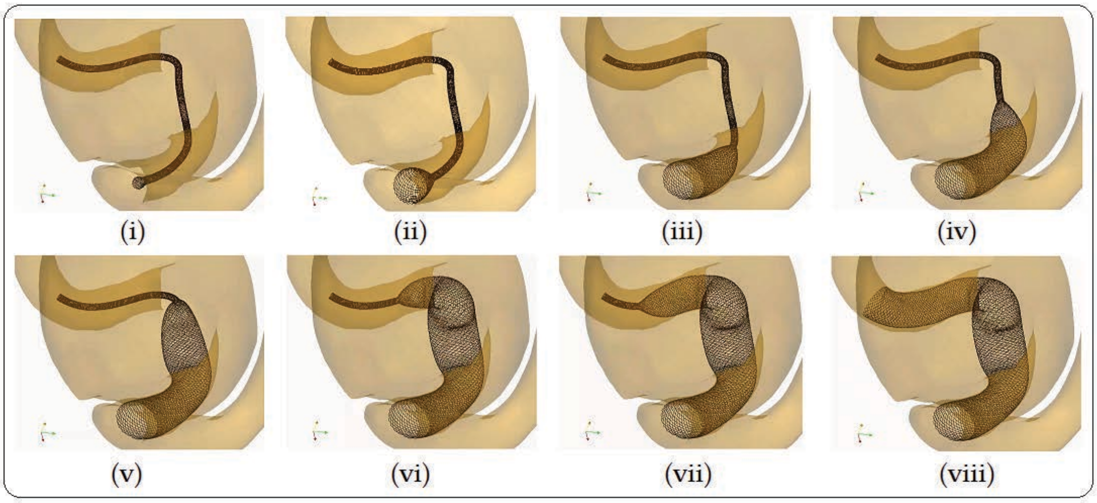

Figure 2. A representative virtual stent deployment procedure for the unsuccessfully treated aneurysm. (FD stent size: 4.5 mm, under non-compacted condition; subfigures i to viii: the deployment procedure from stent fully crimped to stent fully expanded.)

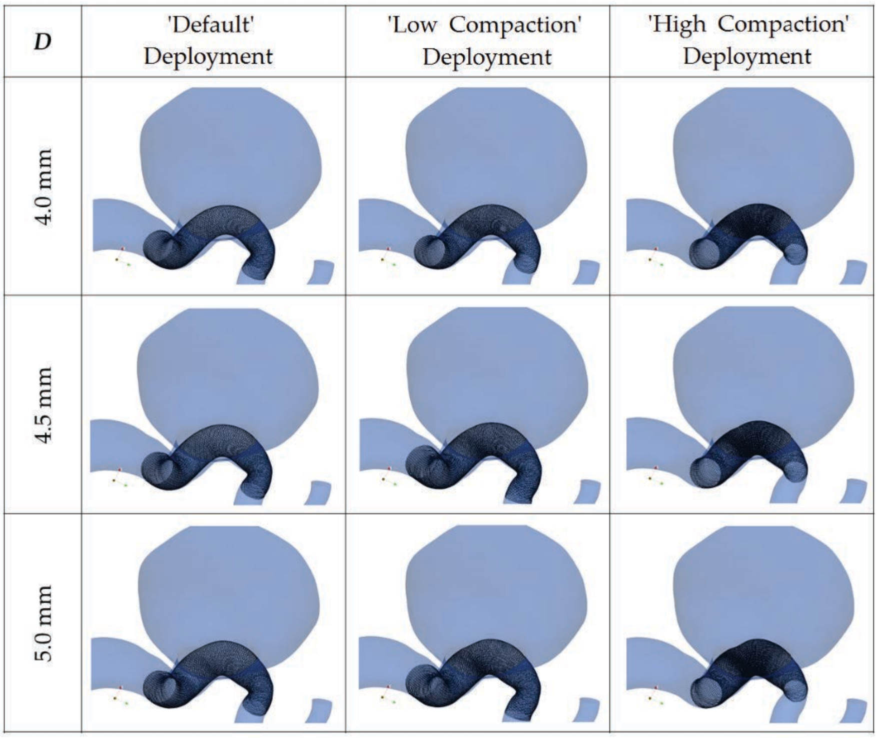

Figure 3. The stent wire configurations of treatments with FD stents of three diameters: 4.0, 4.5, and 5.0 mm, at three compaction levels: 'default' deployment (CPT = 0%), 'low compaction' deployment (CPT = 20%), and 'high compaction' deployment (CPT = 70%) in the successfully treated case.

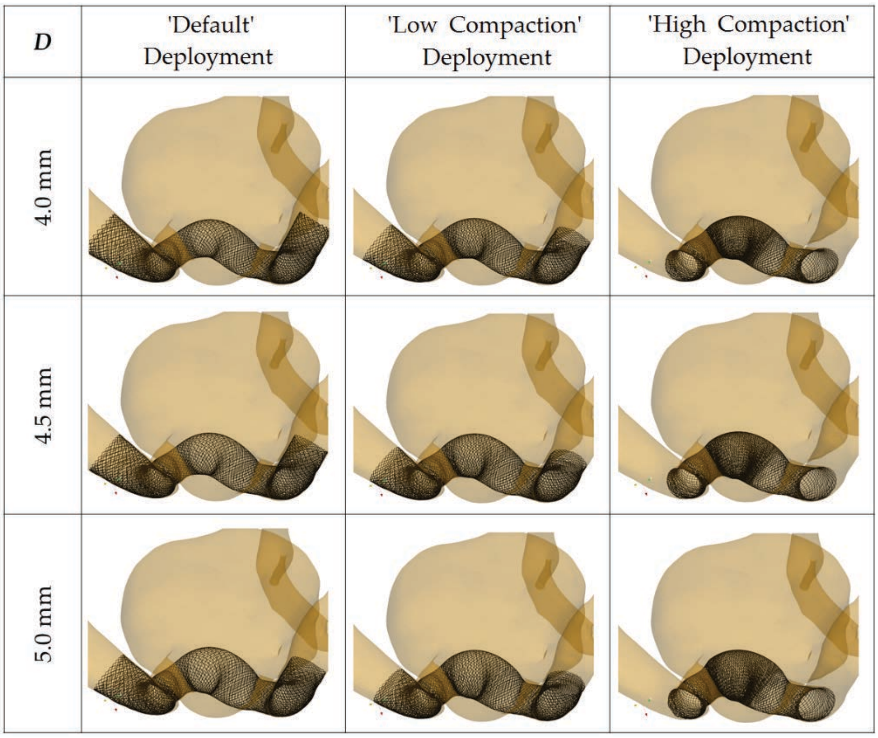

Figure 4. The stent wire configurations of treatments with FD stents of three diameters: 4.0, 4.5, and 5.0 mm, at three compaction levels: 'default' deployment (CPT = 0%), 'low compaction' deployment (CPT = 20%), and 'high compaction' deployment (CPT = 70%) in the unsuccessfully treated case.

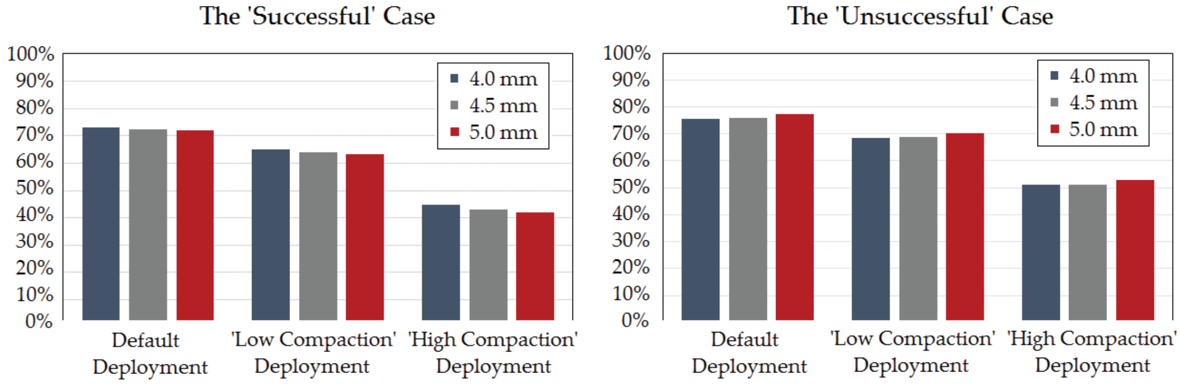

Figure 5. The porosities of the FD stent within the aneurysm ostium measured from treatments with FD stents of three diameters: 4.0, 4.5, and 5.0 mm, at three compaction levels: 'default' deployment (CPT = 0%), 'low compaction' deployment (CPT = 20%), and 'high compaction' deployment (CPT = 70%) in the two cases (successfully treated case at left, unsuccessfully treated case at right).

Discussion

Wire Configurations and Porosities after Deployment with Compaction

We confirmed that stent compaction could decrease the wire porosity across the aneurysm ostium, regardless of the stent size or the recipient aneurysm geometry. The difference between porosities achieved from a low compaction and a high compaction was measured to be 20%. Although the determination of FD stent diameter shows limited effects on stent wire porosity, substantial effects of stent diameter on post-stenting stent shape can be observed.

Different Wire Configurations Obtained in the Successful and the Unsuccessful Case

Observing the post-treatment wire configurations, we found that the stent wires dilate further into the aneurysm ostium in the unsuccessfully treated case. This phenomenon may most likely be due to the morphological characteristics: the unsuccessfully treated case manifests a highly-curved parent artery, compared to the successful one (see Figure 6). Furthermore, the aneurysm in the unsuccessful case was located at the 'apex' of the parent artery curve; treatment with compaction applied may therefore push the FD wires deeper into the aneurysm sac, causing a larger discrepancy between the expected porosity and the obtained one.

In addition, we found a gap between the vascular boundary and the FD stent wires in all treatment scenarios for the unsuccessful aneurysm, whereas no obvious gap was seen in the successful case. This might be an important clue in exploring the reasons why that treatment was ultimately unsuccessful *in vivo*: when blood is flowing through the parent artery, its main stream has a chance to enter the aneurysm sac through the 'gap' (whether or not such gap-induced strong aneurysm inflow eventuates). This point merits further computational fluid dynamics simulations and follow-up DSA scans to gain more specific evidence on such anomalous local haemodynamic behaviour.

If the treating clinicians had have had access to predictive modelling results illustrating the wire configurations and the shape of a virtually deployed FD stent, it is possible that they may have opted to adjust their proposed treatment plan.

Conclusions

Following the definition of compaction ratio developed in this study, we have virtually deployed FD stents of three diameters, with each diameter modelled at three compaction levels, into two patient-specific IAs. Our results indicate that: (i) the porosity differences attributable to device diameter were limited (SD < 2%); and (ii) stent deployment with compaction applied could markedly reduce the wire porosity within the aneurysm ostium (reduction by around 10–30%, depending on the degree of compaction). We observed that the stent wires prolapsed further into the aneurysm sac in the unsuccessful case, most likely due to its geometric characteristics: the unsuccessful case has a highly-curved parent artery.

Treatment rehearsal with a virtual stent deployment simulation would help predict the wire configurations following treatment with a specific device diameter using a given deployment strategy prior to the real treatment, which may be useful in assisting the treating clinicians in determining an optimal treatment plan.

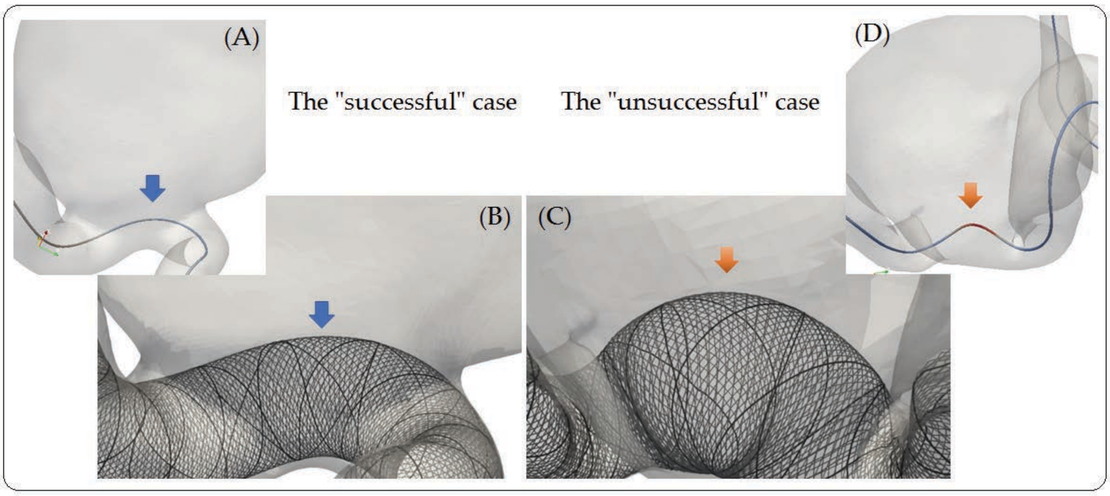

Figure 6. Magnified view of FD wire dilation into the aneurysm lumen. Subfigures A and B show the FD wires after deployment in respectively the successful and the unsuccessful cases; subfigures C and D depict the centrelines extracted from the respective aneurysm geometry for comparison.

Acknowledgements

This study was supported by the ImPACT Program of Council for Science, Technology and Innovation (Cabinet Office, Government of Japan), the Macquarie University Research Excellence Scholarship (iMQRES, No. 2015257), and the Australian Research Council Linkage Projects (Grant ID: LP130100423). The authors would like to thank Dr. Xi 'George' Zhao for many fruitful discussions and valuable suggestions regarding the programming of wall-touch detection.

References

[1] Brisman, J.L., Song, J.K., and Newell, D.W. (2006) Cerebral aneurysms. *New England Journal of Medicine* **355** (9), 928–939.

[2] Sforza, D.M., Putman, C.M., and Cebral, J.R. (2009) Hemodynamics of cerebral aneurysms. *Annual Review of Fluid Mechanics* **41** (1), 91–107.

[3] Zanaty, M., Chalouhi, N., Tjoumakaris, S.I., Rosenwasser, R.H., Gonzalez, L.F., and Jabbour, P. (2014) Flow-diversion panacea or poison? *Frontiers in Neurology* 5.

[4] Qureshi, A.I., Janardhan, V., Hanel, R.A., and Lanzino, G. (2007) Comparison of endovascular and surgical treatments for intracranial aneurysms: an evidence-based review. *The Lancet Neurology* **6** (9), 816–825.

[5] Cebral, J.R., Mut, F., Raschi, M., Hodis, S., Ding, Y.-H., Erickson, B.J., et al. (2014) Analysis of hemodynamics and aneurysm occlusion after flow-diverting treatment in rabbit models. *American Journal of Neuroradiology* **35** (8), 1567–1573.

[6] Ma, D., Xiang, J., Choi, H., Dumont, T.M., Natarajan, S.K., Siddiqui, A.H., et al. (2014) Enhanced aneurysmal flow diversion using a dynamic push-pull technique: an experimental and modeling study. *American Journal of Neuroradiology*.

[7] Makoyeva, A., Bing, F., Darsaut, T.E., Salazkin, I., and Raymond, J. (2013) The varying porosity of braided self-expanding stents and flow diverters: an experimental study. *American Journal of Neuroradiology* **34** (3), 596–602.

[8] Gentric, J.-C., Salazkin, I., Gevry, G., Raymond, J., and Darsaut, T. (2015) Compaction of flow diverters improves occlusion of experimental wide-necked aneurysms. *Journal of NeuroInterventional Surgery* neurintsurg-2015-012016.

[9] Lubicz, B., Collignon, L., Raphaeli, G., Pruvo, J.-P., Bruneau, M., De Witte, O., et al. (2010) Flow-diverter stent for the endovascular treatment of intracranial aneurysms: a prospective study in 29 patients with 34 aneurysms. *Stroke* **41** (10), 2247–2253.

[10] Spranger, K. and Ventikos, Y. (2014) Which Spring is the best? comparison of methods for virtual stenting. *IEEE Transactions on Biomedical Engineering* **61** (7), 1998–2010.

[11] Spranger, K., Capelli, C., Bosi, G.M., Schievano, S., and Ventikos, Y. (2015) Comparison and calibration of a real-time virtual stenting algorithm using finite element analysis and genetic algorithms. *Computer Methods in Applied Mechanics and Engineering* **293**, 462–480.

[12] Peach, T.W., Spranger, K., and Ventikos, Y. (2015) Towards predicting patient-specific flow-diverter treatment outcomes for bifurcation aneurysms: from implantation rehearsal to virtual angiograms. *Annals of Biomedical Engineering*.

[13] Zhang, M., Li, Y., Zhao, X., Verrelli, D.I., Chong, W., Ohta, M., et al. (2017) Haemodynamic effects of stent diameter and compaction ratio on flow-diversion treatment of intracranial aneurysms: a numerical study of a successful and an unsuccessful case. *Journal of Biomechanics* **58**, 179–186.